Imperial College
London

# VALIDATING A RESTRAINED MOLECULAR DYNAMICS MODEL FOR $\alpha$-SYNUCLEIN

Martina Oliver Huidobro

Supervisors: Dr. Alfonso De Simone

Carlos Navarro Payà

Final Year Project for Bsc Biochemistry
Department of Life Sciences
Imperial College London

7 June, 2019

**Abstract**

$\alpha$-synuclein is a 140-residue intrinsically disordered protein, whose oligomers have been proved to be toxic, causing death of dopaminergic neurons and ultimately leading to Parkison's disease. Although extensive research has been carried on this protein, detailed information on the structural behaviour as well as functional or pathological mechanisms of $\alpha$-synuclein is still lacking. This is mainly because both the dynamical nature and the conformational variability of its 3 different regions make it hard to obtain meaningful structural insights from traditional structural studies. To address this issue, a Molecular Dynamics model has been developed to explore detailed mechanisms of $\alpha$-synuclein using simulations. In this project, we have tested the model and compared the simulation results to experimental data from the literature. This model seems to be mostly in accordance with the experimental data and describes successfully some of the behaviours of $\alpha$-synuclein. Once refined, this computational tool will allow us to further understand the functional and pathological behaviours of $\alpha$-synuclein.

# Contents

# 1 Introduction

## 1.1 $\alpha$-synuclein: Parkison's Disease

$\alpha$-synuclein is a 14 KDa intrinsically disordered protein (Galvagnion et al. 2015). It has been shown to be one of the major components of Lewy Bodies (Fusco, Pape, et al. 2016). Lewy bodies, are intra-neuronal aggregates which develop in patients with Parkison's Disease (PD) and other synucleinopathies (Fusco, Sanz-Hernandez, et al. 2018). In the case of PD, these Lewy bodies are located in the substantia nigra, a region where dopaminergic neurons are found (Chinta and Andersen 2005). Aggregates of $\alpha$-synuclein are believed to cause neuronal death by forming pores in the membrane that increase permeability and allow the flux of ions, hence disrupting the cell's equilibrium. However, rather than the Lewy bodies, it has been shown that the toxic form of $\alpha$-synuclein is as an oligomer (Brown 2010; Cremades et al. 2012). This loss of dopaminergic neurons, leads to key symptoms in PD such as motor dysfunction (Bartels et al. 2010).

## 1.2 Physiological roles

$\alpha$-synuclein is mainly found in the presynaptic terminals of neurons (Fusco, De Simone, Gopinath, et al. 2014). Although its physiological function is still largely unknown, it has been shown to be involved in the regulation of synaptic vesicle (SV) supply from the reserve pool as well as a chaperone in the SNARE complex formation for vesicle fusion (Fusco, Pape, et al. 2016). However, the presence of $\alpha$-synuclein in other regions such as heart tissues or red blood cells, indicate it might have other non-neurological functions (Fusco, Pape, et al. 2016; Fusco, De Simone, Arosio, et al. 2016). Such variety of potential functions is possible due to the dynamical nature of $\alpha$-synuclein, which allows for a wide range of conformations.

## 1.3 $\alpha$-synuclein's membrane-binding dynamics

$\alpha$-synuclein can adopt several conformations, including a $\beta$-sheet stabilised amyloid in Lewy Bodies, a disordered monomer in solution, and partially helical when membrane bound (Wang et al. 2016). It is worth noticing that $\alpha$-synuclein has a more compact structure than other disordered proteins of similar lenght (Dedmon et al. 2005).

The ability of $\alpha$-synuclein to bind membranes is driven by favourable energetics as a result of its amphipatic sequence. This sequence is formed by 7 imperfect repeats of 11 residues that allow the formation of a class A2 lipid-binding $\alpha$-helix from residues 1-90 (**Figure 1a**). The result of this is an $\alpha$-helical structure with hydrophobic residues being buried inside the membrane, positive residues interacting with phosphate groups and negative residues in contact with water. As seen in **Figure 1b** for residues 1-25, negative residues (Glu and Asp) are found on top, positive residues are found on the sides (Lys) and hydrophobics are found on the bottom. This behaviour has been observed in Fusco, De Simone, Gopinath, et al. 2014 and Fusco, De Simone, Arosio, et al. 2016, where NMR paramagnetic relaxation enhancement experiments showed hydrophobic residues being spatially close to carbon 5 in the lipid tail of the bilayer. In these experiments, hydrophilic residues do not insert the membrane. These repeats are responsible for the helicity of $\alpha$-synuclein. They are regular at the very N-terminus, and progressively become more irregular as we go down the sequence (Figure 1b) (Fusco, Sanz-Hernandez, et al. 2018). This decrease in amphipatic partitioning, leads to the distinction of 3 dynamical regions in $\alpha$-synuclein

with different membrane affinities: the N-terminus, central and C-terminus region (**Figure 1a**). The population of helical structure for each region can be measured using Chemical Exchange Saturation Transfer. This experiment showed that in the presence of SUVs, 86% of the protein population had an $\alpha$-helical N-terminus and decreasing percentage for the central region and C-terminus respectively (Fusco, De Simone, Gopinath, et al. 2014).

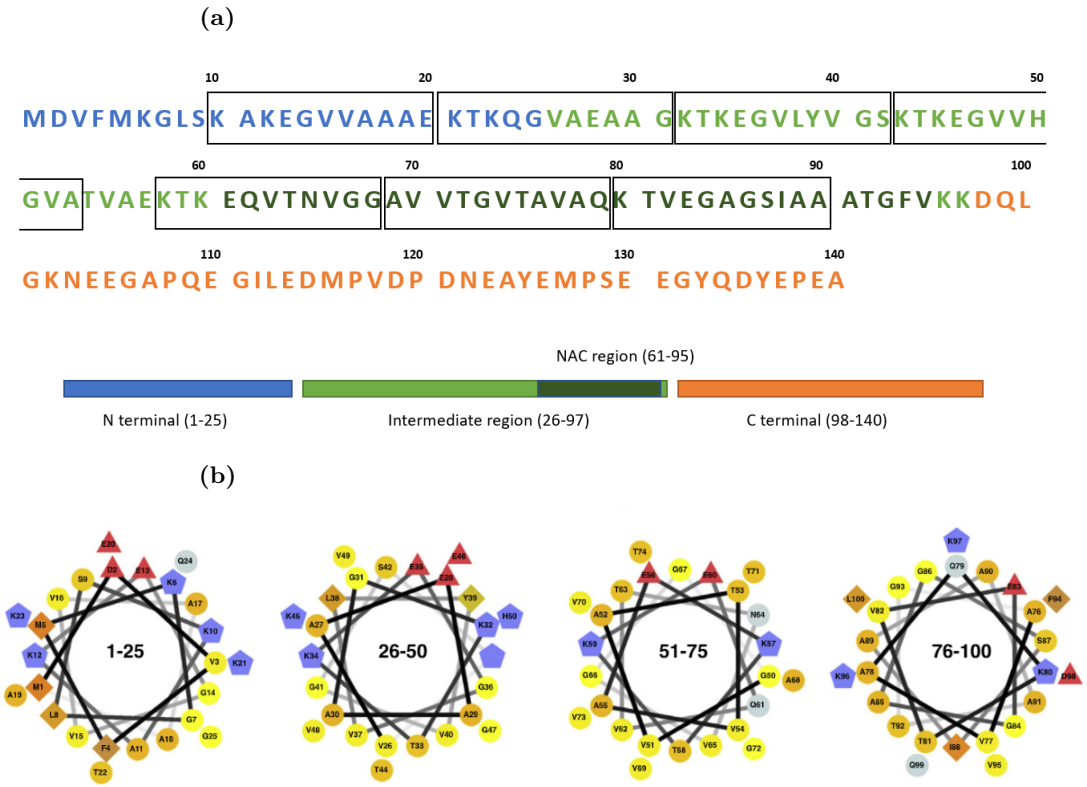


**Figure 1: Sequence features of $\alpha$-synuclein and its distinct regions. a)** Full $\alpha$-synuclein sequence with 7 imperfect repeats separated with black boxes. The three distinct dynamical regions of the protein are shown including the N-terminus (blue), the central region (light green) with the NAC region inside (dark green) and finally the C-terminal region (orange). **b)** Adapted from Fusco, Sanz-Hernandez, et al. 2018. Helical projection of $\alpha$-synuclein's sequence showing amphipatic partitioning from 1-100 (region where helix is formed). The projections are divided into four segments showing different amphipatic partitioning. Negatively charged residues are shown in red, positively charged are shown in purple or grey and the rest are shown in orange or yellow.

In its membrane bound form, the 140-residue $\alpha$-synuclein presents three dynamical regions with different structural and dynamical properties. The N-terminal region spans residues 1-25.

It has been shown to anchor phospholipid membranes and is commonly found as an inserted amphipatic helix that facilitates binding to the membrane (Fusco, De Simone, Gopinath, et al. 2014). The central region, residues 26-97, undergoes constant order-disorder transitions as it fluctuates between bound (helical) and unbound (disordered) states. This region is able to act as a lipid-sensor, having different affinities for different lipid compositions and membrane curvatures. This central region also contains the NAC (non-amyloyd $\beta$ component), which forms the core of $\alpha$-synuclein fibrils upon aggregation. Mutations that over expose the NAC facilitate aggregation into fibrils (Fusco, De Simone, Arosio, et al. 2016). In addition, these exposing mutations also promote vesicle-vesicle interactions mediated by $\alpha$-synuclein through a double-anchor mechanism, previously proposed by (Fusco, De Simone, Arosio, et al. 2016; Fusco, Pape, et al. 2016). This shows how sensitive the equilibrium between physiological and pathological properties of $\alpha$-synuclein are (Fusco, Sanz-Hernandez, et al. 2018). Finally, the C-terminal spanning residues 98-140, is mainly disordered and associates weakly with the membrane and some positively charged metal ions such as Ca2+ (Lautenschläger et al. 2018). It is believed to be involved in stabilisation of the protein as well as a chaperone due to its unstructured nature (Sang et al. 2002). All these regions are shown in **Figure 2**.

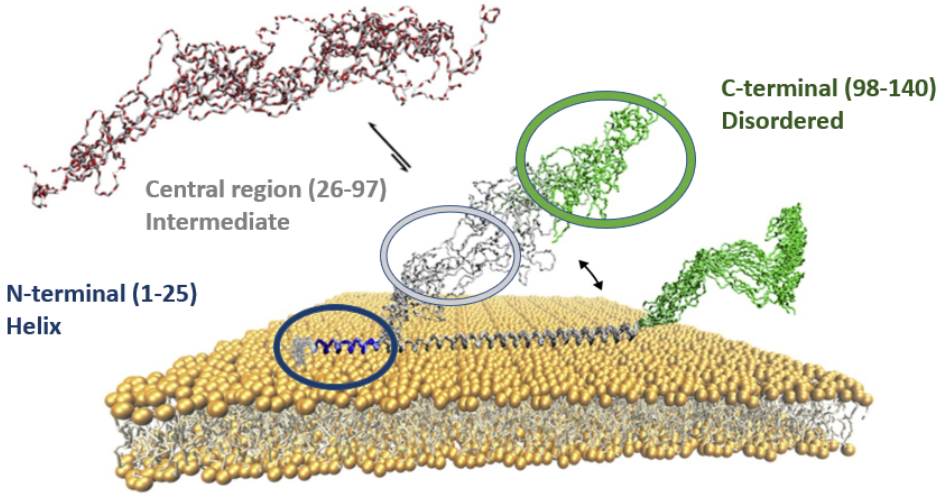


**Figure 2: $\alpha$-synuclein's membrane bound structure and monomeric soluble disordered structure.** Figure adapted from (Fusco, Sanz-Hernandez, et al. 2018). The monomeric soluble $\alpha$-synuclein is shown in red. As a membrane bound protein, $\alpha$-synuclein is depicted with its N-terminal region shown in blue, central region shown in grey and C-terminal region shown in green. Fluctuations in the binding and unbinding of the central region are observed.

Further research is required to understand $\alpha$-synuclein's binding mechanism and conformational transitions. It is worth noticing that subtle changes in affinity of the NAC region can promote either its potential physiological role or its aggregation pathway. This highlights the importance of obtaining a detailed mechanism for its interaction with the membrane (Fusco, Sanz-Hernandez, et al. 2018). Both the intrinsically disordered properties and the conformational transitions of this protein make it hard to obtain meaningful structural insights from traditional structural studies such crystallography or classic NMR (Fusco, De Simone, Arosio, et al. 2016). Hence, alternative tools are required for the in-depth study of $\alpha$-synuclein's behaviour.

## 1.4 Molecular Dynamics

Molecular dynamics (MD) has been shown to be a good alternative approach to structural studies (Karplus and McCammon 2002). MD is a computer simulation method used to study the motion of particles in a system. At every time-step of the simulation, the Newtonian equations of motion are calculated giving as an output new coordinates and a velocity vector (Lindahl 2008). This method allows us to explore the conformational space of different molecules including proteins.

MD simulations started as atomistic simulations, where the system is described at an atomistic resolution. However, running atomistic simulations on complex systems such as proteins and lipids, can become become very computationally demanding. A technique commonly used in this field to reduce computational cost is the use of coarse grained (CG) models. (Siewert J. Marrink et al. 2019). In CG simulations, the degrees of freedom and number of particles in the system are reduced, decreasing the computational power compared to atomistic models. (Periole and Siewert Jan Marrink 2013). This is done by representing groups of atoms (around 4 heavy atoms) as an individual bead (interaction centre) with a particular polarity and hydrogen-bonding capabilities (Periole and Siewert Jan Marrink 2013). When choosing your simulation approach between atomistic and CG for your simulation, the number of atoms and the length of the simulation needs to be considered. While computational cost is decreased with a CG approach allowing to explore larger timescales, resolution and detail at the atomic level is lost (Lindahl 2008). CG approaches have proven to be useful to model the dynamics of lipids and systems with proteins embedded in membranes (Lindahl 2008). For the purpose of studying $\alpha$-synuclein in a membrane environment, a CG approach will be used so longer timescales can be explored in a feasible way.

One of the advantages of MD is that it provides details on the motion of individual particles, and hence can help to answer specific questions about the system that cannot be solved experimentally (Karplus and McCammon 2002). Furthermore, being able to control parameters (such as lipid composition, salt concentration, temperature) allows us to explore how these factors affect the system (Karplus and McCammon 2002). Theoretically, MD gives a potential resolution that is much better than experimentally approaches. However, this resolution is totally dependent on the realism and accuracy of the force field (i.e. set of parameters and equations used to calculate the potential energy of particles in the system), and also the computational power available. The advantages that MD provides over classic structural approaches above mentioned, make it an adequate alternative tool to study $\alpha$-synuclein.

CG Force Fields (FF) like Martini can be used to study Biomolecular systems. However, this force field has some disadvantages when working with some disordered proteins. Firstly, the Martini FF was parameterised using experimental data and atomistic models describing globular

proteins. This leads to disordered proteins behaving more like globular than they should (Das et al. 2018). For $\alpha$-synuclein, this results in its hydrophobic residues being buried inside the core, resulting in a ball shaped structure which is not in accordance with experimental data.

To solve this, an in-house definition of disordered and helical conformations of $\alpha$-synuclein was made by a PhD student in De Simone's group. Backbone angles and dihedrals are redefined to obtain more realistic values, similar to the ones seen in the literature. To obtain a flexible definition of these angles and dihedrals, restraints are introduced through an energy potential function. Specific equilibrium values for helical and disordered conformations were used. In this model, the conformation of $\alpha$-synuclein (helical or disordered) has to be defined a priori so the model can implement different functions for the helical and disordered conformations.

### 1.5 Aims and Objectives

The aim of this project is to test and validate this newly developed MD model, ensuring that is in accordance with experimental results. In this report, we tested the behaviour of these two defined conformations in the presence of a lipid membrane. For a concrete validation of the model, we replicated the experimental setups from Vamvaca et al. 2009 where 6 N-terminus deletion variants were tested for membrane binding affinity. The N-terminus region of the protein and a phospholipid bilayer were simulated and the relative membrane binding propensity was measured. Our simulations showed similar results, meaning we can continue refining our restrained MD model to increase accuracy for studying $\alpha$-synuclein.

## 2 Methods

### 2.1 GROMACS package and Martini forcefield

The Coarse-Grained Molecular Dynamics (CG-MD) model developed tested in this report, is a modification of the GROMACS simulation package. The modification allows us to restrain the backbone angle and dihedral values. From the coordinates obtained during the simulation, the angles and dihedrals between backbone beads are calculated. These serve as an input to

an energy potential function which determines the strength and direction of the force applied to those backbone angles and dihedrals. This force applied at each timestep, is aimed to force more realistic angles in the backbone of $\alpha$-synuclein's structure. In this initial CG-MD model developed, the protein conformation (helical or disordered) has to be defined a priori. This is necessary as depending on the conformation defined, different energy potential functions with different values for the angles and dihedrals will be used. The energy potential function will then bias the backbone towards a helical or a disordered conformation.

For all simulations, the Martini 3 force field was used with GROMACS 4.6.7 simulation software in a Linux environment (Tieleman et al. 2008; Van Der Spoel et al. 2005). As previously explained, the CG model represents an average of four heavy atoms with a single interaction centre (except with ring-like structures). This bead can be polar, non-polar, apolar or charged; and it has different hydrogen-bonding capabilities (donor, acceptor, both or none) as well as degrees of polarity (1 to 5) (Periole and S.-J. Marrink 2013). Each protein residue has a backbone bead and depending on the residue, zero to four side-chain beads. Two different types of forces are represented in this force field: nonbonded interactions and bonded interactions. The first one, is represented by the Lennard Jones potential which depends both on the distance of two particles and on the type of particles (polar, non polar, apolar and charged). In addition, charged particles interact via a Culombic energy potential function. The second one, bonded interactions, are represented with a set of energy potential functions affecting angles ( $\theta_{\mathrm{ijk}}$) and dihedrals ($\theta_{\mathrm{ijkl}}$) **(Figures 5 and 7)**. These functions have a weak force constant, allowing flexibility of the chemical bonds and the chain.

## 2.2 Setting up the Coarse Grained system.

Firstly, sequences for the N-terminus (1-25 residues) of the 6 variants and the wild-type used in Vamvaca et al. 2009 were used to build pdb files of peptides with Chimera software (Pettersen et al. 2004). The methods described below and shown in **(Figure 4)** were carried out with

the same conditions for the 7 different constructs. The atomistic structure was coarse-grained using the python script martinize.py, which produces a CG structure (.pdb) and a topology file (.top). The topology file contains information on the bead types, backbone and sidechain angles, dihedrals and bonds. All the default backbone angles generated in the top file were deleted to later impose our own restraints.

Next, the whole system was built in a 15x15x15 nm box, using the python script *insane.py*. The system includes 1 $\alpha$-synuclein, 19641 water beads, 108 Cl- and 322 Na+ ions and a complex lipid bilayer with 8639 lipids. Initially, the protein was placed 40nm away from the membrane plane. The bilayer consists of a 5:3:2 molar ratio of 1,2-Dioleoyl-sn-glycero-3-phosphoethanolamine (DOPE), 1,2-dioleoyl-sn-glycero-3-phospho-L-serine (DOPS) and 1,2-dioleoyl-sn-glycero-3-phosphocholine (DOPC) lipids, which mimic synaptic vesicles (SV) in terms of curvature and composition (Fusco, Pape, et al. 2016).

## 2.3 Minimisation and equilibration

The system was energy minimised in vacuum and in the presence of temperature and pressure by running short simulations at 310K of 0.01 and 0.04 ns respectively. The main difference between the vacuum and the normal minimisation was that no temperature and pressure coupling was used in the vacuum minimisation. The minimisations were carried to avoid potential steric clashes from the initial structure provided. In the normal minimisation, Berendsen thermostat and barostat were used for temperature and pressure coupling respectively, to ensure that these 2 parameters remain constant throughout the simulation. In all steps using temperature and pressure coupling, relaxation times ($\tau$) for temperature and pressure were of 2 and 12 ps respectively, which means the temp and pressure values are recalibrated every $\tau$ ns (Lemkul 2018). The pressure applied of 1 bar was isotropic, which means its is equal in all directions allowing more flexibility of the system during the minimisation steps.

The following steps where carried out for every variant, at every temperature (ranging from 310-450K), both for helical and disordered conformations, which as explained previously, were defined a priori. The timestep used until now is 10 ps. Every subsystem was equilibrated during

a 15ns simulation, ensuring that the area per lipid converged. In this case, a velocity-rescale thermostat and a Berendsen barostat were used, and an initial velocity was calculated for every temperature. For this step, the pressure (1bar) is coupled semiisotropically, which means pressure is exerted both on the x-y and the Z plane respectively. This allows the x-y plane to deform independently from the Z axis, which is key for maintaining the membrane structure (Lemkul 2018).

This final production run starting from the minimised and equilibrated system was run for 2400 ns, a value that was chosen to ensure convergence of the system. The timestep used was 20 fs. In this production run velocity-rescale thermostat was used to maintain the temperatures (ranging from 310-450) and Parrinello-Rahman barostat was used to keep the semiisotropic pressure of the system at 1bar. A schematic workflow of the whole process is represented in **Figure 3**.

Overall, 210 simulations of 2400 ns where produced. This included the combination of 6 variants and the wild-type's N-terminus used in Vamvaca et al. 2009 (**Figure 4**) , ordered and disordered conformations for each and 15 temperatures ranging from 310 to 450K.

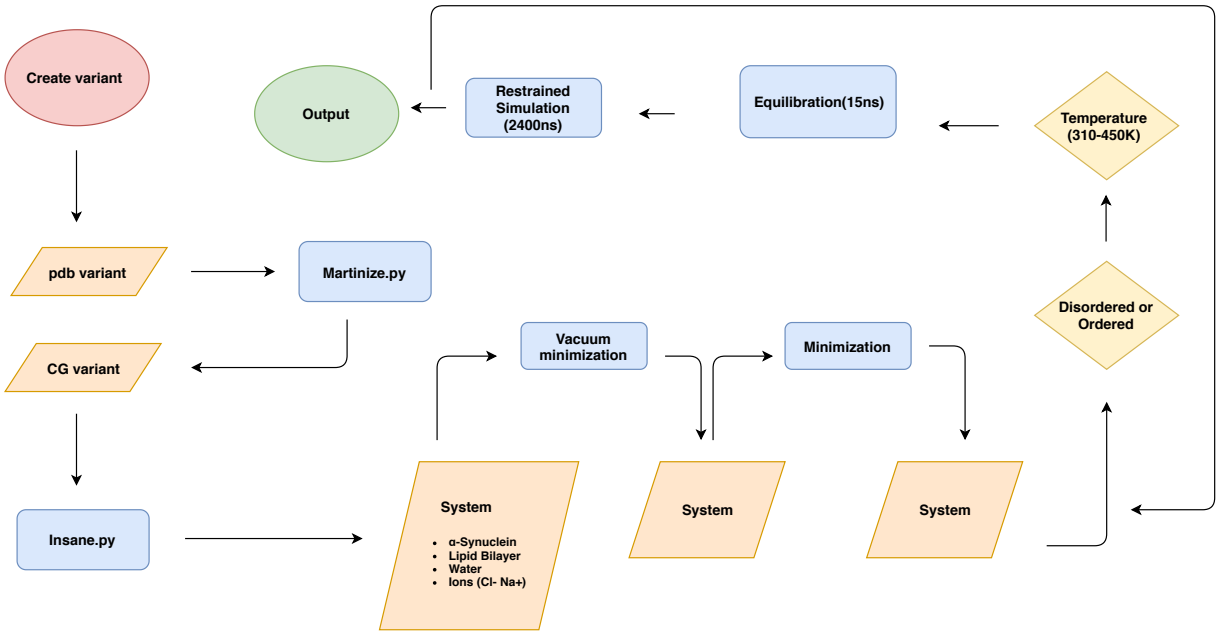


**Figure 3: Schematic workflow of the simulation setup.** The initial input is depicted in a red. Output/Input objects are shown in orange. Processes including steps of the simulation setup and the simulation run are shown in blue. Decision steps are depicted in yellow.

## 2.4 Spatial definition of angles and dihedrals using an energy potential function

Some extra energy potential functions were added to the GROMACS 4.6.7 package. This modification was done to obtain more accurate simulations of the protein by imposing restraints on the angles and dihedrals. Previously, the defined angles generated with the insane.py script were deleted so we could impose our own constraints. Our restraints were introduced through an energy potential function, where the angles and dihedrals obtained at each timestep of the production run were used as an input. This energy potential function determines the force applied to angles and dihedrals so they tend towards a more realistic value. In this initial MD model, the conformation (helical or disordered) has to be defined a priori as different values for the angles and dihedrals will be targeted.

First, the coordinates obtained in the simulation where used to calculate the angles (i,j,k)

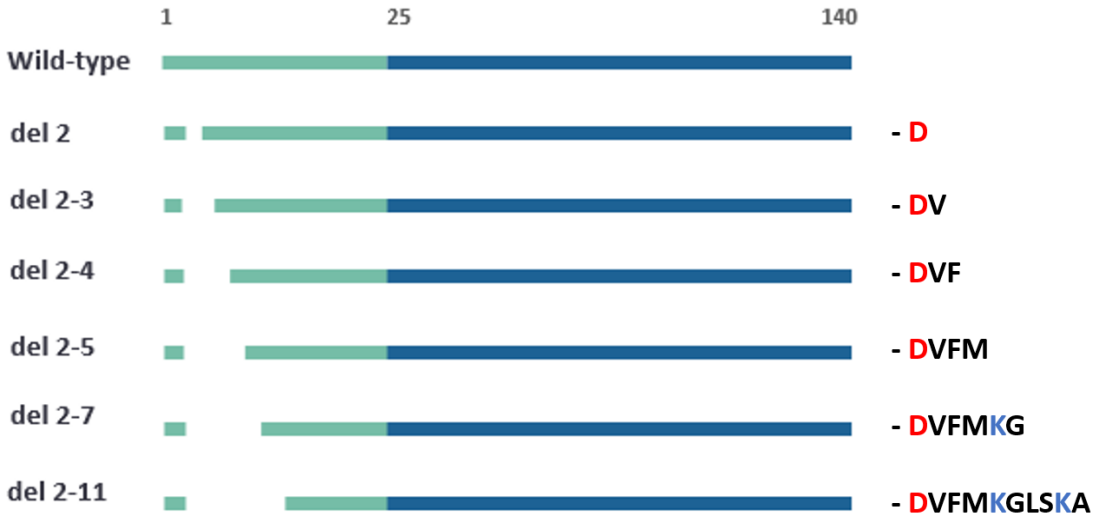


**Figure 4: $\alpha$-synuclein wild-type and deletion variants tested in the simulation**. The N-terminus is shown in green, from residues 1-25. The rest of the sequence including the central and C-terminus is depicted in blue. The aminoacids deleted for each variant are shown on the right of each variant. Negatively charged aminoacids are shown in red, positively charged are shown in blue and the rest are shown in black.

and dihedrals (i,j,k,l) between backbone beads shown in **Figure 5 and 7** respectively.

### 2.4.1 Angles

The cosine of the angle $\theta_{\mathrm{ijk}}$ formed by two vectors $\mathbf{r}_{\mathrm{ij}}$ and $\mathbf{r}_{\mathrm{kj}}$ pointing towards a common atom j can be expressed as

$$cos\theta_{ijk} = \frac{\mathbf{r}_{ij} \cdot \mathbf{r}_{kj}}{|r_{ij}||r_{kj}|} \tag{1}$$

The angle was obtained with the ArcCosine function. $\theta_{\mathrm{ijk}}$ is then used to calculate the energy potential ($\mathrm{V_A}$) with the following the energy potential (EP) function. This EP function is given by the following Gaussian function plotted in **Figure 6a**.

$$V_A = -K_{ijk} e^{\frac{-(\theta_{ijk}-\theta_{exp})^2}{\sigma}} \tag{2}$$

$K_{ijk}$ is the force constant (defined as 50Kj/mol) of this potential function, $\theta_{ijk}$ is the angle value measured experimentally which represents the minima of this function and $\sigma$ represents the width of the Gaussian well. For helical and disordered conformations, $\theta_{ijk}$ is 96°and 127°respectively and $\sigma$ is 14 °and 28 °respectively, allowing greater flexibility for the disordered conformation. To obtain the force acting on the particle i, we calculated the negative derivative of the EP function mentioned above with respect to the particle i expressed as a vector $\mathbf{r}_i$ **(Figure 6b)**. Using the chain rule, we can express this force function with the following equation

$$F_i = -\frac{\delta V_A}{\delta \mathbf{r}_i} = -\frac{\delta V_A}{\delta \theta_{ijk}} \frac{\delta \theta_{ijk}}{\delta \mathbf{r}_i} \tag{3}$$

This way, every angle is recalculated at each time-step by applying this force, which will bias it towards a more experimentally realistic angle.

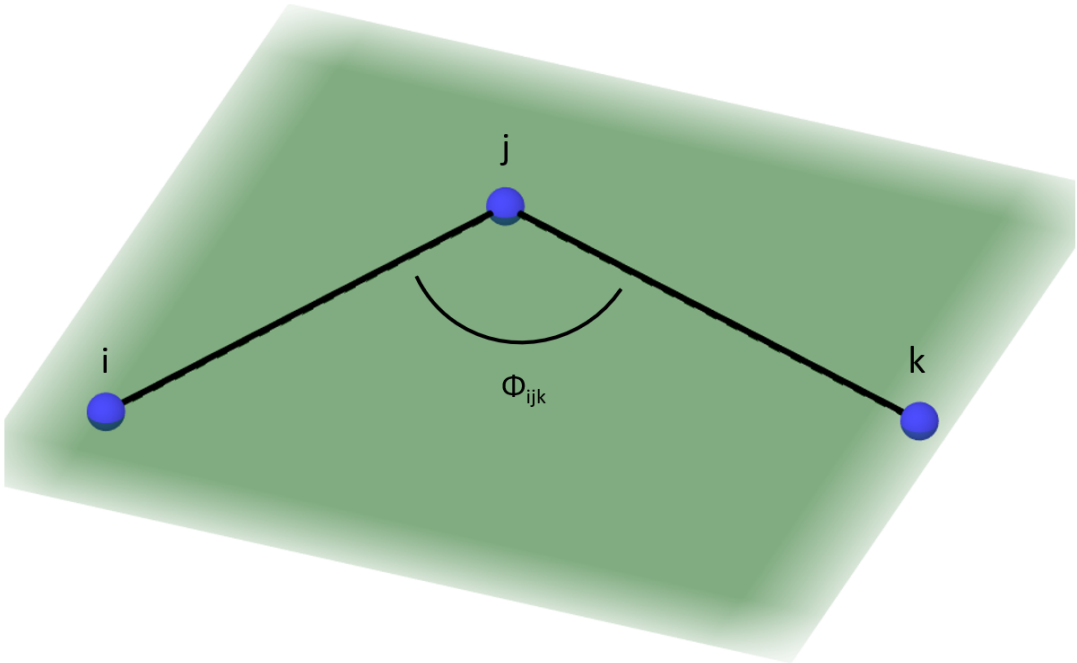


**Figure 5: Backbone angle $\theta_{ijk}$.** The angle $\theta_{ijk}$ is formed by three consecutive backbone particles i, j and k (blue). The covalent bonds are depicted as black lines. The three particles form the plane ijk, shown in green.

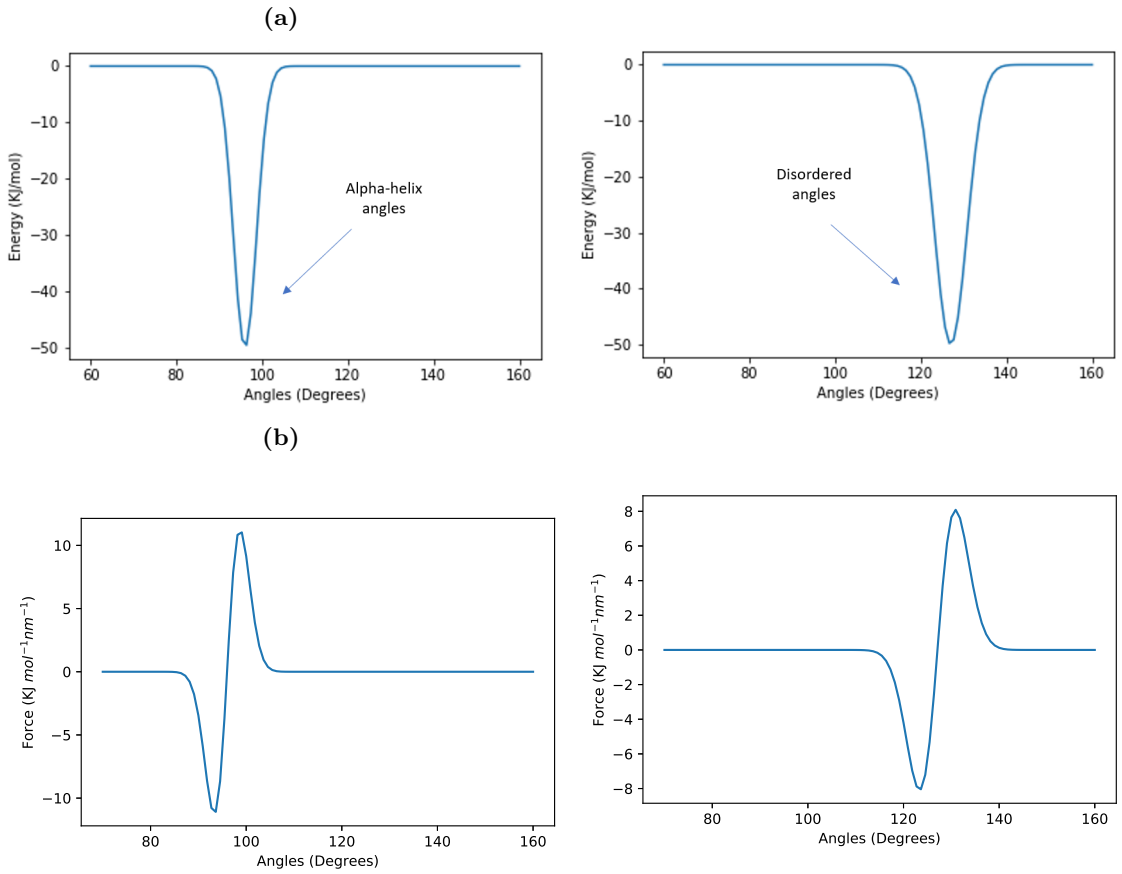


**Figure 6: Energy potential and Force functions used to restrain angles and dihedrals** **a)** Energy potential function defined as a Gaussian Function with a minima located at the experimental values for angles (96°and 127°respectively for helical and disordered conformations). On the left, the energy potential function for the helical conformation. On the right, the energy potential function for the disordered angles. A wider "well" can be observed for the disordered conformation. **b)** The Force function defined as the derivative of the energy potential function where negative and positive values refer to the different senses of the force vector. For input angles, a different force will be applied depending on the energy potential and force functions.

### 2.4.2 Dihedrals

A similar process is used to redefine dihedrals. The dihedral is the angle defining the relative position of four consecutive backbone particles (**Figure 7**). In this case, $\theta_{\text{ijkl}}$ is defined as the angle between the normal vectors $\mathbf{n}_{\text{ijk}}$ and $\mathbf{m}_{\text{jkl}}$ of the two planes passing through ijk and jkl

respectively. These vectors are defined as

$$n = r_{ij} * r_{jk} \tag{4}$$

$$m = r_{jk} * r_{lk} \tag{5}$$

and the cosine of $\theta_{\text{ijkl}}$ is defined by

$$cos\theta_{ijkl} = \frac{m \cdot n}{m * n} \tag{6}$$

The energy potential functions is defined with the Gaussian function

$$V_A = -K_{ijk} e^{\frac{-(\theta_{ijkl} - \theta_{conformation})^2}{\sigma_{conformation}}} \tag{7}$$

and the force is calculated with

$$F_i = -\frac{\delta V_A}{\delta cos\theta_{ijk}} \frac{\delta cos\theta_{ijk}}{\delta r_i} \tag{8}$$

The backbone dihedrals are calculated and a force is applied in a similar fashion that the backbone angles described previously.

## 2.5 Defining Binding Propensity and data analysis

The simulations produced .xtc files for every variant, conformation and condition. These .xtc files are the output trajectory file, which contains coordinates and velocity vectors for every time-step of the production run. All the data obtained from the simulations was handled with python, using the structure and data analysis library Pandas. For every variant in a specific conformation, a matrix was generated with the binding propensities of each residue at every temperature. Our

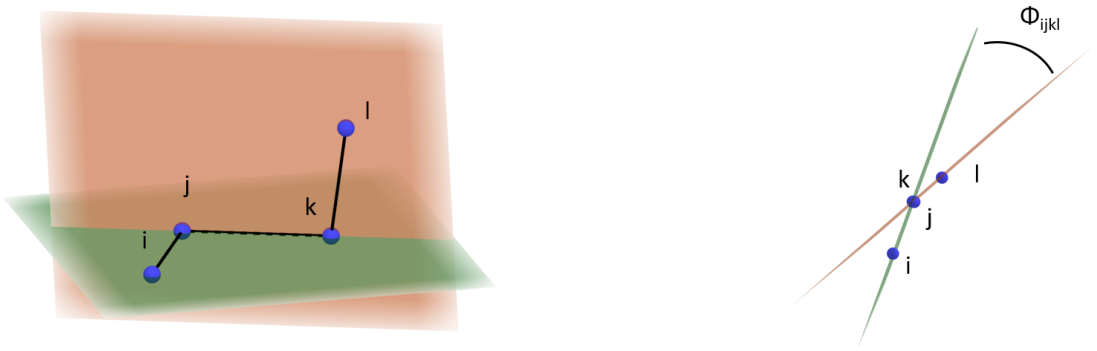


**Figure 7: Dihedral dihedral $\theta_{\mathbf{ijkl}}$.** The dihedral $\theta_{\mathrm{ijkl}}$ is formed by four consecutive backbone particles i,j,k and l (blue). The convalent bonds between backbone residues are shown as black lines. The dihedral is defined as the angle between the two planes formed by ijk (green) and jkl (orange).

definition of binding propensity is the average time spent bound at the membrane. Our cutoff for 'bound' is that the residue is located at a distance $<$ 1nm from the closest $PO4^-$ particle, which describes the polar side of the membrane. At every time-step, we explored whether the residue was bound or unbound and calculated the average by dividing the number of time frames 'bound' (Bound) by the total number of timeframes (Total). The following definition of Relative Binding Propensity will be used for all graphs of the results section:

$$Relative\ Binding\ Propensity = \frac{Bound}{Total} \tag{9}$$

With temperatures as columns, and residues as rows, a relative binding propensity was defined for every cell in the matrix. These binding propensities were used to generate all plots in the results section that compare the behaviour of wild-type and different variants.

## 2.6 Convergence of the system

Convergence of the system was tested by comparing the same results for the first half timeframe and for the second half. This was done to make sure that the simulation time was enough to obtain all the relevant data.

# 3 Results

## 3.1 Comparison of Wild Type $\alpha$-synuclein in helical and disordered conformations

In **Figure 8** we observe that both conformations bind strongly until residue 11. After residue 11, the binding propensity of the disordered conformation decreases noticeably even at lower temperatures **(Figure 8b)**. The helical conformation remains mostly the same with a small decrease in residue Q24 (**(Figure 8a)**. We can also observe that higher temperatures have a lower binding propensity for both conformations, as was expected. Additionally, we can notice a clear oscillation in binding propensity every 4 residues for the helical conformation.

**(a)** Wild-type Helical conformation

**(b)** Wild-type Disordered conformation

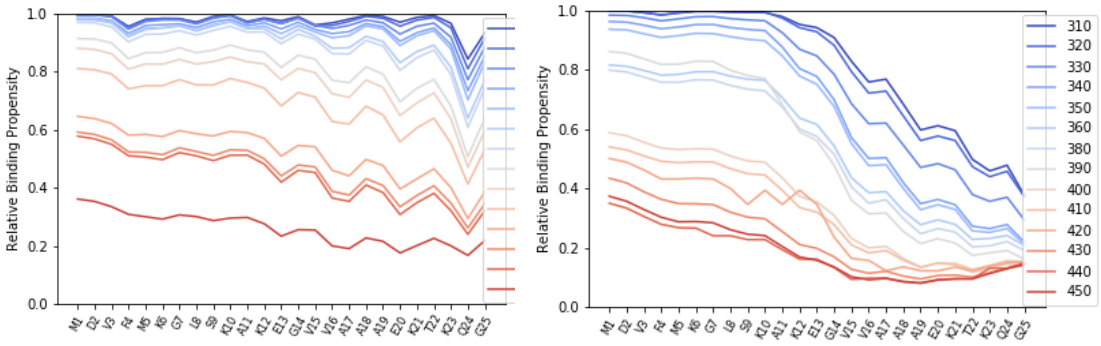


**Figure 8: Relative Binding Propensity for residues 1-25 in $\alpha$-synuclein.** Relative binding propensity is shown for the helical simulation (**a)**) and the disordered simulation (**b)**) across all temperatures. Temperatures (K) for every simulation are shown with a colour-scale: blue colours represent lower temperatures and red colours show higher temperatures ranging from 310 to 450K.

To further understand how the different segments of the N-terminal behave, we look at their binding propensity under different temperatures. Melting curves were plotted for both conformations with the N-terminal split in two (1-11 and 12-25, blue and orange respectively) (**Figure 9)**. Overall, all segments have decreasing binding affinity as temperature increases following a sigmoidal curve that is fitted using MATLAB. The melting curves show that the helical conformation (**Figure 9a**) binds more stably than the disordered (**Figure 9b**), showing

high binding propensities at high temperatures. Furthermore, segment 12-25 (orange), has a lower binding propensity than segment 1-11 (blue).

## 3.2 Comparison of wild type and 6 deletions variants of $\alpha$-synuclein

The 6 deletion variants replicating the experimental setup in Vamvaca et al. 2009 are compared using melting curves for each individual variant. Again, the N-terminus is split in two to study the behaviour of both segments separately. As with the wild-type melting curves discussed previously, we can see that in all graphs the first segment 1-11 (blue) binds more tightly to the membrane than the second segment 12-25 (orange) **(Figure 10 to 15)**. Del2 has a higher binding propensity than the wild-type, reflected in residues 1-11 (blue). This is true both for helical and disordered conformations **(Figure 10a)**. A similar behaviour is replicated in Del2-3. In this case, the binding of the segment 1-11 in disordered conformations is slightly higher and the binding for segment 12-25 in helical conformation is slightly lower than in the previous deletion (Del2) **(Figure 11)**. Del2-4 has a similar binding profile for residues 1-11 to the wild-type for the helical conformation. For residues 12-25, the wild-type is still slightly higher than Del2-4 **(Figure 12a)**. For the disordered conformation, the binding propensity is higher than in the wild-type for both segments, showing a similar profile to Del2 and Del2-3 **(Figure 12b)**. Del2-5 shows a similar binding profile than the wild-type both for helical and disordered conformation **(Figure 13)**. The disordered conformation has lost binding stability compared to the previous deletion (Del2-4). In Del2-7, the segment 1-11 in the disordered conformation has an increase in binding affinity. The helical conformation and the disordered 12-25 region remain the same as the wild-type **(Figure 14)**. Finally, the Del2-11 has lower binding propensities than the wild-type both for helical and disordered conformation along the whole sequence **(Figure 15)**. However, the helical conformation suffers a bigger decrease in binding propensity than the disordered conformation.

**(a)** Wild-type Helical

**(b)** Wild-type Disordered

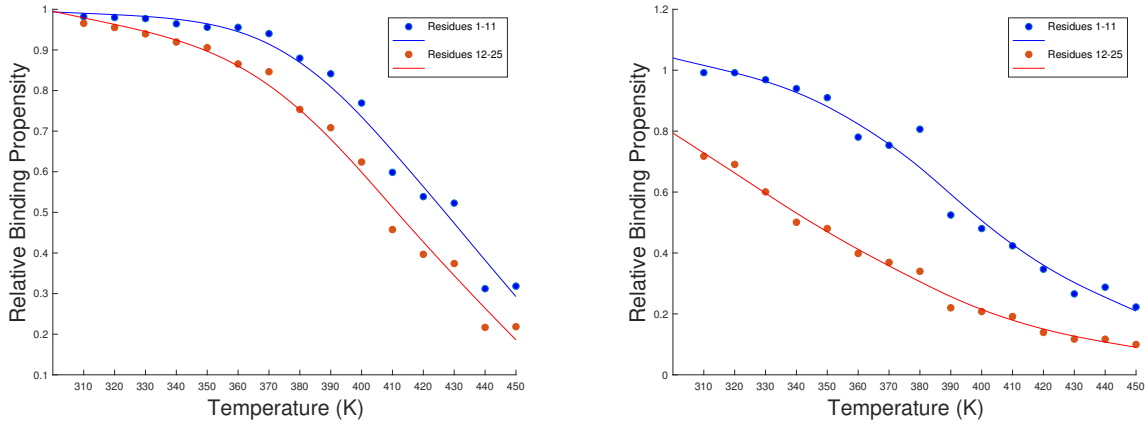


**Figure 9: Melting curve for $\alpha$-synuclein's N terminus**. The 1-25 sequence is split in half, resulting in two segments 1-11 and 12-25. Melting curve for residues 1-11 is shown in blue and for residues 12-25 is shown in red. A sigmoid fit is traced to smooth the melting curves. Helical conformation is shown in the left (**a**)) and disordered conformation is shown in the right (**b**)).

**(a)** Del2 Helical

**(b)** Del2 Disordered

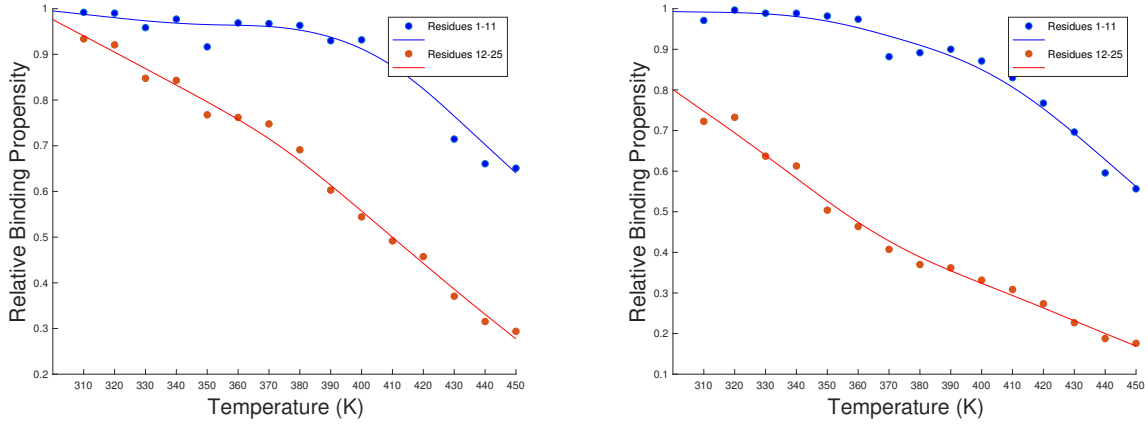


**Figure 10: Melting curve for Del2**. The 1-25 sequence is split in half, resulting in two segments 1-11 and 12-25. Melting curve for residues 1-11 is shown in blue and for residues 12-25 is shown in red. A sigmoid fit is traced to smooth the melting curves. Helical conformation is shown in the left (**a**)) and disordered conformation is shown in the right (**b**)).

**(a)** Del2-3 Helical

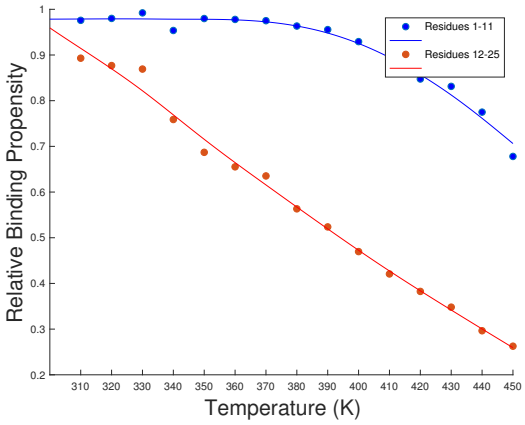


**(b)** Del2-3 Disordered

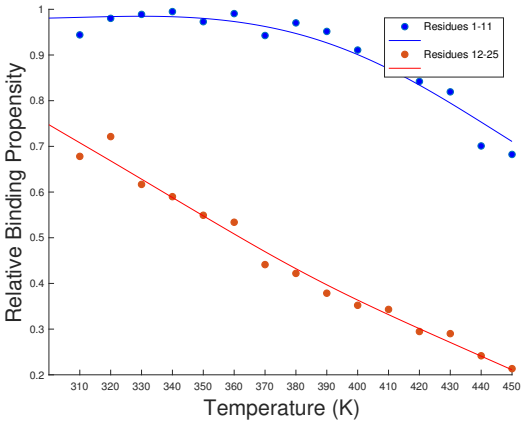


**Figure 11: Melting curve for Del2-3**. The 1-25 sequence is split in half, resulting in two segments 1-11 and 12-25. Melting curve for residues 1-11 is shown in blue and for residues 12-25 is shown in red. A sigmoid fit is traced to smooth the melting curves. Helical conformation is shown in the left (**a**)) and disordered conformation is shown in the right (**b**)).

**(a)** Del2-4 Helical

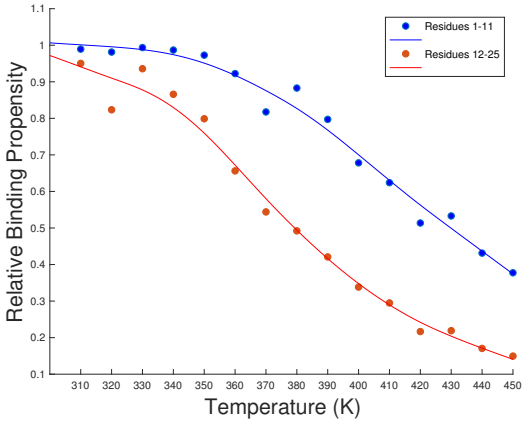


**(b)** Del2-4 Disordered

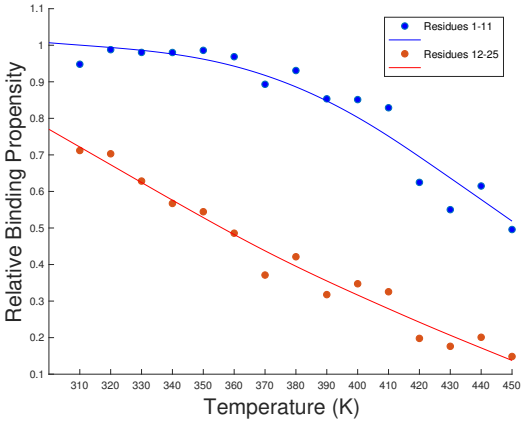


**Figure 12: Melting curve for Del2-4**. The 1-25 sequence is split in half, resulting in two segments 1-11 and 12-25. Melting curve for residues 1-11 is shown in blue and for residues 12-25 is shown in red. A sigmoid fit is traced to smooth the melting curves. Helical conformation is shown in the left (**a**)) and disordered conformation is shown in the right (**b**)).

**(a)** Del2-5 Helical

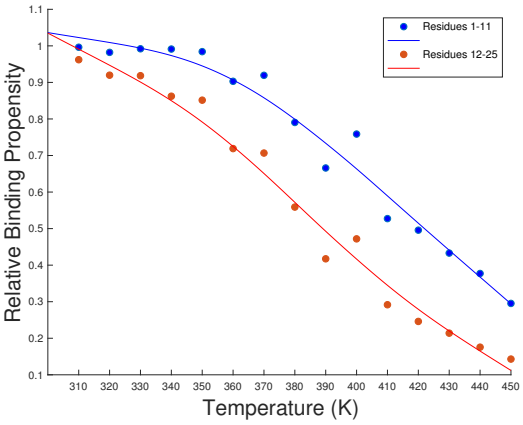


**(b)** Del2-5 Disordered

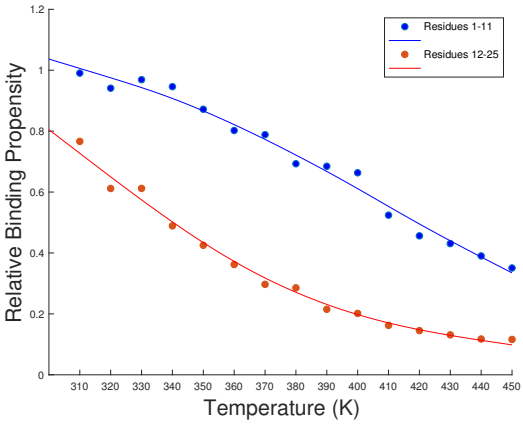


**Figure 13: Melting curve for Del2-5**. The 1-25 sequence is split in half, resulting in two segments 1-11 and 12-25. Melting curve for residues 1-11 is shown in blue and for residues 12-25 is shown in red. A sigmoid fit is traced to smooth the melting curves. Helical conformation is shown in the left (**a**)) and disordered conformation is shown in the right (**b**)).

**(a)** Del2-7 Helical

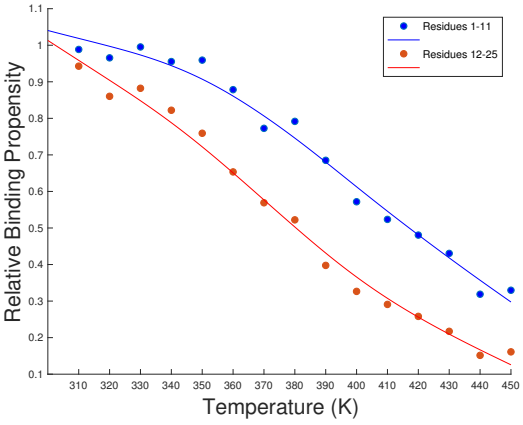


**(b)** Del2-7 Disordered

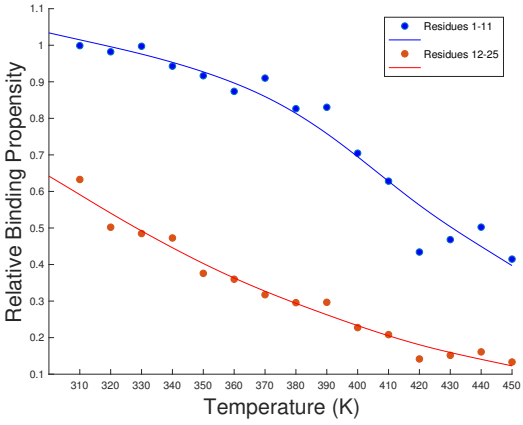


**Figure 14: Melting curve for Del2-7**. The 1-25 sequence is split in half, resulting in two segments 1-11 and 12-25. Melting curve for residues 1-11 is shown in blue and for residues 12-25 is shown in red. A sigmoid fit is traced to smooth the melting curves. Helical conformation is shown in the left (**a**)) and disordered conformation is shown in the right (**b**)).

**(a)** Del2-11 Helical

**(b)** Del2-11 Disordered

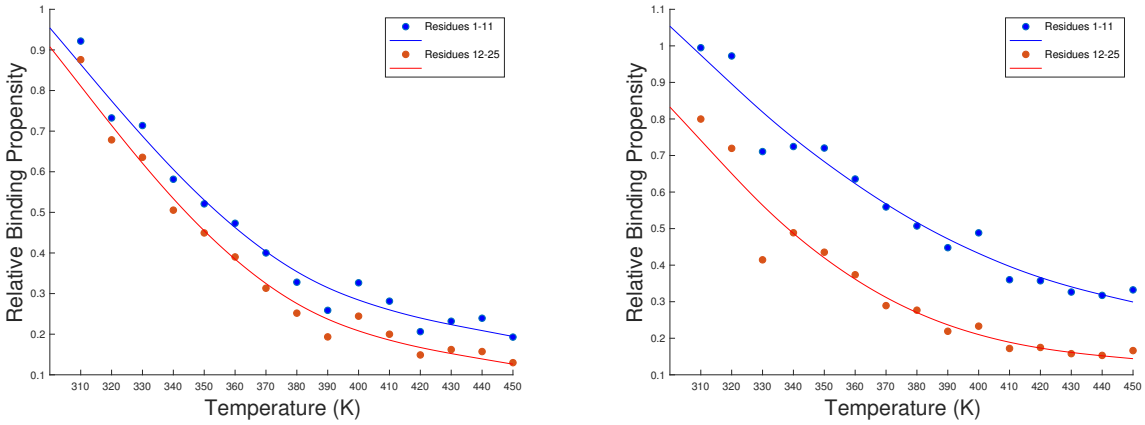


**Figure 15: Melting curve for Del2-11**. The 1-25 sequence is split in half, resulting in two segments 1-11 and 12-25. Melting curve for residues 1-11 is shown in blue and for residues 12-25 is shown in red. A sigmoid fit is traced to smooth the melting curves. Helical conformation is shown in the left (**a**)) and disordered conformation is shown in the right (**b**)).

For every variant in both conformations, the average binding propensity for all residues at all temperatures is calculated. Overall, the average relative binding propensity is higher in the helical conformation **(Figure 17)**. Del2 is higher than the wild-type in both conformations, which also happens in the experimental data from Vamvaca et al. 2009 **(Figure 16)**. In the helical conformation, there is a decrease in binding propensity as more residues are removed, with a significant drop for the last truncation Del2-11. This pattern is also seen in the experimental data. For the disordered conformation, Del2-3 is higher than Del2-3 **(Figure 18)**. Subsequent deletions follow the same behaviour as in the helical conformation, where increasing number of deleted residues leads to decrease in binding propensity.

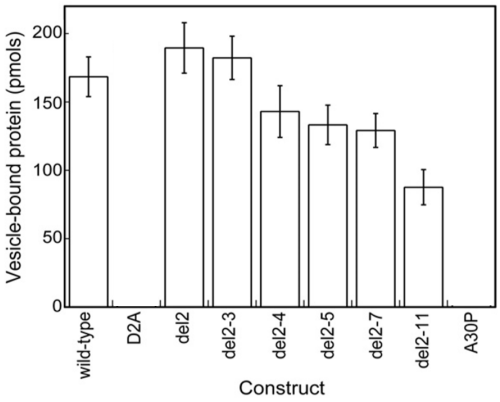


**Figure 16: Experimental binding propensities of $\alpha$-synuclein's wild-type and different deletion variants.** Figure adapted from Vamvaca et al. 2009. The height of the bars represents the vesicle bound protein (pmols), which will be compared to our relative binding propensity.

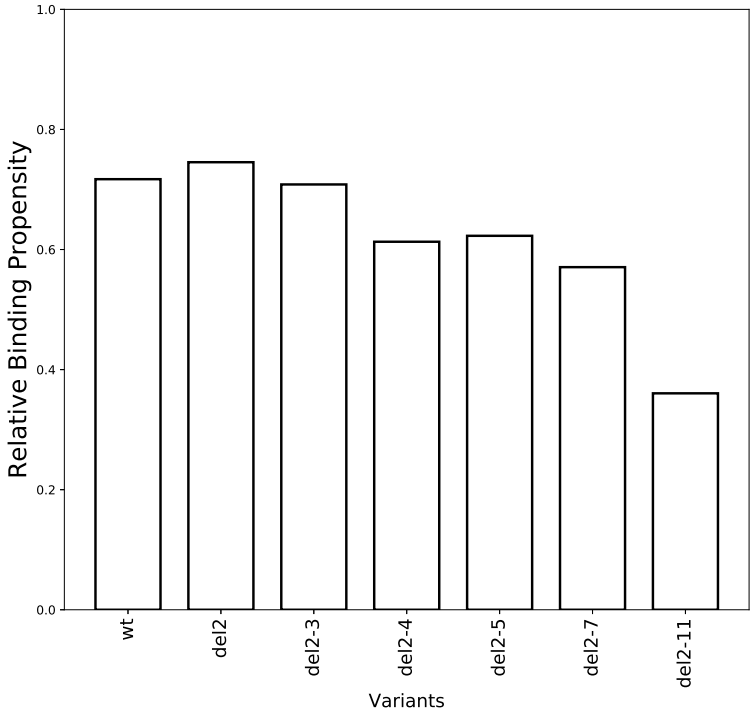


**Figure 17: Simulated binding propensities of helical wild-type and different deletion variants.** The height of the bars represents the relative binding propensity of the variants to the membrane.

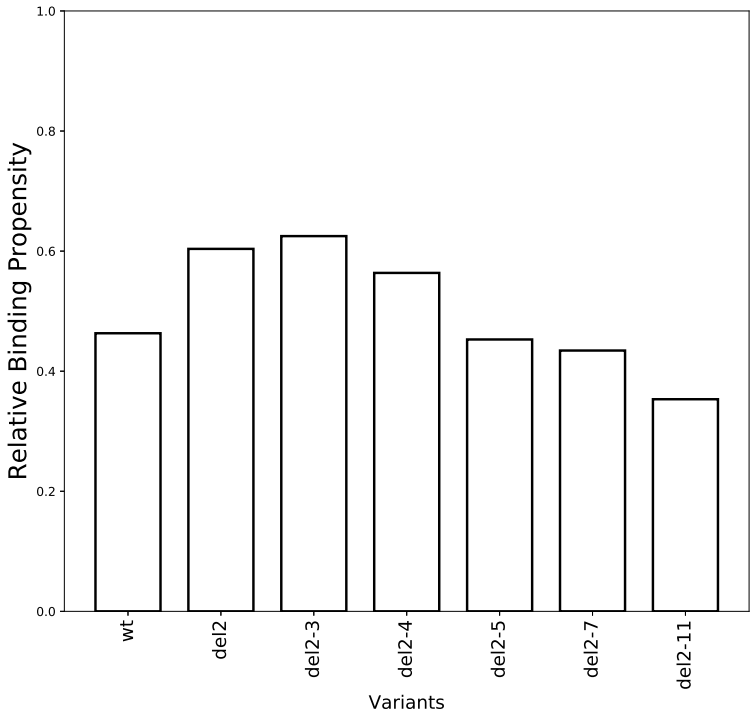


**Figure 18: Simulated binding propensities of disordered wild-type and different deletion variants.** The height of the bars represents the relative binding propensity of the variants to the membrane.

## 3.3 Convergence

The results for both halves of the simulation are almost the same meaning they have converged and no more time is required. However, temperature 440 behaves in a different manner, meaning it hasn't converged appropriately and more simulation time was needed for this one. No statistical data with replicates can be obtained from this MD approach. Hence, convergence is used to ensure the relevance of the data.

**(a)** 1-1200ns (First half).

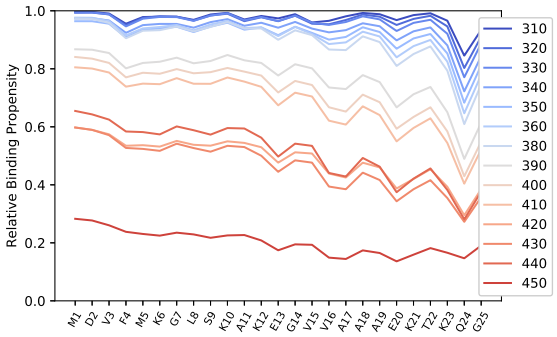


**(b)** 1200-2400ns (Second half).

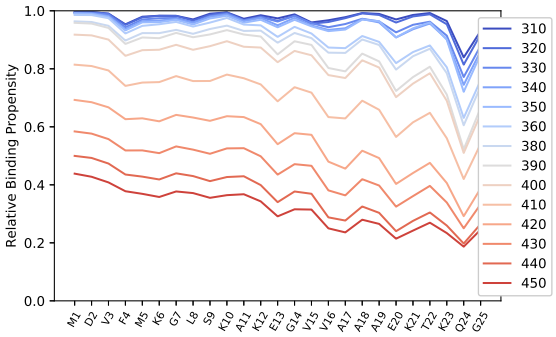


**Figure 19: Convergence Results.** Relative Binding propensity for residues 1-25 is used to test convergence. Same graphs are plotted for **a)** showing the simulation's results for the first half of the simulation (1-1200ns) and **a)** showing exactly the same for the second half of the simulation (1200-2400ns).

# 4 Discussion

The dynamical nature of $\alpha$-synuclein, makes it hard to study its behaviour through classical structural studies. To address this issue, a restrained molecular dynamics model has been developed, that can approximate the behaviour of $\alpha$-synuclein. Validation of this model was achieved by comparing the protein behaviour in our simulations to experimental data in the previous literature. Furthermore, insights on the mechanism of $\alpha$-synuclein's membrane binding where obtained.

To assess the relevance of our model to study $\alpha$-synuclein, we first focused on the wild-type's binding behaviour. As previously described in the introduction, it is well established that $\alpha$-synuclein's N-terminal is mainly found in a helical conformation when membrane bound (Fusco, De Simone, Gopinath, et al. 2014). This indicates that when simulating the N-terminal, the membrane binding stability of a helix should be higher than that of a disordered region. In the simulations here discussed, higher binding propensity is seen for the helical conformation when comparing both wild-type conformations in figure x.

Previous literature has shown that the first 11 residues of $\alpha$-synuclein have a different behaviour than those from 12-25, with increased binding to the membrane (Maltsev et al. 2012; Bartels

et al. 2010). For this reason, we decided to study the two segments separately and we observed a higher binding propensity for the first 11 residues. This pattern is both observed in the wild-type simulation and in the 6 deletion variants, both for helical and disordered conformations (Figures 8 to 15 and Figures 1 to 6 in Supplementary. Materials). Interestingly, this difference in binding propensity between the first and the seconds segment is smaller in the helical conformation. This might be because in the tighter helical conformation, the whole sequence (1-25) forms a helix, meaning it behaves similarly from start to end. However, in the less compact disordered conformation, the flexibility allows both regions of the sequence to behave differently, and hence one segment ca be bound while the other one is unbound. This pattern shows how conformation is key for the binding propensity of $\alpha$-synuclein.

The amphipatic nature of the sequence described in the literature (Fusco, Sanz-Hernandez, et al. 2018), can be seen in **Figure 8a** for the wild-type and in the supplementary material for all the other variants, where affinity for the individual residues is shown. The 4 residue oscillation occurs as in the helix, polar residues facing upwards have a relative lower binding propensity while the hydrophobic residues have a higher one (e.g. downwards peak in relative binding propensity for E13 and E20 which are found in the polar side of the helix). Additionally, a big drop in binding propensity is seen in residue 24 for the helical conformation. This is because the peptide generated with Chimera, has a negative charge at the end of the C-termini (residue 25). This negative charge pulls out the helix from the membrane and therefore the polar Q24 found on the opposite side of the sequence **Figure 1b**) gets very separated from the membrane, hence showing a drop in relative binding propensity. This drop in binding propensity at Q24 should not occur in the full length $\alpha$-synuclein as it does not have this artificial positive charge. The wild-type data discussed above, seems to be in accordance with the literature following the expected behaviour of $\alpha$-synuclein. This indicates the restrained MD model is potentially suitable to study $\alpha$-synuclein.

For a more concrete validation of the model, simulations were carried for $\alpha$-synuclein deletion variants already tested in Vamvaca et al. 2009. All deletions follow an expected behaviour when considering the residues that have been deleted. Comparison of the deletions has been done by using **Figures 9 to 15** as well as **Figured 7** from the Supplementary material, where melting curves for all residues are compared in the same graph.

In Del2, a negatively charged Asp is removed, explaining the increase in binding propensity: as the membrane's surface is negatively charged by phosphate groups, removing a negative charge gets rid of the electrostatic repulsion, hence increase binding propensity. This phenomena occurs irrespective of conformation. This is seen both in melting curves (**Figure 10**) and in the histogram (**Figure 17 and 18**).

When deleting an additional hydrophobic Val (Del2-3), the binding propensity for residues 12-25 in the helical conformation decreases slightly. This deletion doesn't affect the first segment of the helix but the second one. This might be because removing a residue might disrupt the repeat and therefore the helix formation, which ultimately affects the binding propensity of downstream residues. However, the increase in binding propensity for residues 1-11 in the disordered conformation might be explained by the disordered conformation being less inserted in the membrane and therefore hydrophobic residues being unfavourable for membrane binding. Hence, when you remove Val, binding propensity increases in the disordered conformation (**Figure 11**).

For Del2-4, an extra bulky hydrophobic Phe is removed. This causes the helical conformation to get a similar binding profile than the wild-type, with 12-25 segment having a bigger decrease in binding propensity than the 1-11 segment. This might mean that the bulky residue was probably required in the formation of a helix, and hence removing it destabilises it and the binding of the protein. This also explains why in helical, 12-25 is more affected than 1-11 segment, as probably 1-11 is less affected when forming a helix due to its highly amphipatic sequence. Furthermore, in this case, the disordered region is unaffected by the removal of Phe, further proving that this Phe was mainly key for helix formation (**Figure 12**).

In Del2-5, an hydrophobic methionine is removed, showing a decrease in biding propensity for both conformations, but specially for the disordered conformation, giving them both similar binding profiles to the wild-type variant (**Figure 13**). The deletion of this hydrophobic residue does not seem to have any major chemical effects, but overall losing another residue in the N-terminus seems to be unfavourable for binding propensity.

In Del2-7, both a positively charged Lys and a Gly are additionally removed. In this case, deleting these two extra aminoacids decreases the binding propensity for the helix and for the disordered segment 12-25 compared to the wild-type. This result can be explained by the disappearance of the electrostatic attraction between the membrane's surface and the Lys (**Figure 14**). Additionally,

it can also be explained by the fact that the first residues are key for membrane binding, so removing them generally should decrease binding propensity of the peptide. However, the increase in binding propensity for the 1-11 segment of the disordered conformation is an unusual result that might be a consequence of the inaccuracy of the model.

For the last deletion (Del2-11), where an additional four aminoacids are removed (Leu, Ser, Lys and Ala) we should observe the biggest decrease in binding propensity for both helical and disordered conformations compared to wild-type. This would be a result of removing 10 key residues of the N terminal decreases noticeably the binding stability of the peptide. As expected, both conformations have a considerable drop in relative binding propensity compared to the wild-type, showing the importance of these 11 residue sequence in membrane binding for any conformation (**Figure 15**). However, it is worth noticing that there is a bigger difference between the wild-type and the last truncation in the helical conformation, meaning that removing these residues not only alters the overall chemical affinity but also affects the helix formation. Comparing the melting curves of all these deletion variants, allows us to acknowledge not only the importance of an alpha helix for membrane association, but also the importance of the hydrophobic and positively charged aminoacids in the initial 11 residue sequence.

After comparing all deletion variants with each other, we can compare our simulation results with the experimental results of Vamvaca et al. 2009. Overall, the histogram showed in this paper shows a similar pattern to the histograms resulting from our simulation results. The wild-type has a lower binding propensity than Del2 for both conformations, due to the removal of the negative charge (Asp) (**Figure 17 and 18**) . This feature is also observed in the experimental histogram (**Figure 16**), showing that our MD model fits the experimental behaviour of $\alpha$-synuclein. For the helical conformation, we can see a progressive decrease in binding propensity as we remove more and more residues with a big drop in the last Del2-11, which is also in accordance with experimental data. However, Del2-5 seems to have a higher binding propensity than expected, which might results from the inaccuracy of the model. For the disordered conformation, we see an increase in binding propensity for the Del2-3, but again the binding propensity decreases the more residues we remove. The disordered conformation is still similar to the results in Vamvaca et al. 2009 showing that the MD model can approximate the behaviour of $\alpha$-synuclein in both

conformations. It is expected that the disordered conformation is in more discord with the experimental data, as in Vamvaca et al. 2009, the N terminal sequence had a higher population in the helical conformation hence being more similar to the MD simulation in helical conformation.

Most of the results discussed above describe an expected behaviour of $\alpha$-synuclein, and are in accordance with the literature and specifically with the Vamvaca et al. 2009 paper. This helps us determine that this initial restrained MD model is a good starting point for developing a relevant computational tool to study $\alpha$-synuclein. However, some results are in discordance with the experimental data and this is because the model still needs refinement.

One of the issues of Martini Force field, is that the conformation of a protein has to be defined a priori, which is why we were simulating helical and disordered conformations of $\alpha$-synuclein separately. This issue, not solved in this MD model, might have caused some discrepancies between the obtained data and the expected results. As discussed previously, $\alpha$-synuclein's regions are highly dynamic and they fluctuate between helical and disordered conformations (specially the central region). This behaviour is not captured in the used MD model.

Next steps in the development of this restrained MD model, will be to introduce a single energy potential function with a helical and a disordered conformation term where the model can determine weather a residue will be helical or disordered without defining it a priori. The conformation of neighbouring residues will be a factor taken into account when defining the conformation of a specific residue, to better mimic $\alpha$-synuclein's behaviour. Hopefully this more complete MD model will allow us to explore the full length of $\alpha$-synuclein with both conformations simultaneously. Such a model will allow us to obtain further insights on membrane binding mechanisms, NAC region behaviour, external factors affecting the protein and potentially exploring the double anchor mechanism where two vesicles are bound by the same $\alpha$-synuclein (Fusco, Pape, et al. 2016).

Even if this MD model needs some further development, it still provided us with some insights on membrane binding mechanisms. Previously in the literature, it had been shown that SVs favoured the helical conformation of $\alpha$-synuclein (Fusco, De Simone, Gopinath, et al. 2014). But the exact mechanism of conformational transition and membrane binding by $\alpha$-synuclein has not yet been elucidated. In **Figure 18** we clearly observe that $\alpha$-synuclein has the ability to bind

membranes in a disordered conformation. Even though it binds with less propensity than the helical conformation, it is still considerable binding. This leads to the conclusion that probably, the N-terminus of $\alpha$-synuclein approaches the membrane in a disordered manner, tethers the membrane in this conformation, and then slowly transitions into a helix driven by the favourable energetics of electrostatic and hydrophobic interactions. Once in a helical conformation, the binding is more stable forming the N-terminal anchor seen in **Figure 2**.

Overall, this first restrained MD model has been shown to be mostly in accordance with the literature and it describes successfully some of the behaviours of $\alpha$-synuclein. These conclusive results will allow us to continue working on this model to improve its relevance for studying $\alpha$-synuclein. Some refinement is needed, so it can simulate both conformations simultaneously for a more integrated model of the protein. A more refined model will give us the possibility of exploring detailed mechanisms of $\alpha$-synuclein, and potentially other membrane binding disordered proteins. However, even with this simplistic MD model, details on the importance of the disordered conformation for the initial approach to SVs were elucidated. This insight on the mechanism of binding, shows the tip of the iceberg in terms of potential of MD for studying $\alpha$-synuclein's behaviour. Hopefully this new tool will give rise to a more detailed understanding of this protein, which will potentially lead to efficient therapeutics to fight against Parkinson's Disease.

## Acknowledgements

I would like to thank sincerely Carlos Navarro Payà for providing support as my day-to-day supervisor and Dr. Alfonso De Simone for providing overall guidance and direction for this project.

Wordcount: 5994 words

# 5 References

# References


Bartels, Tim et al. (2010). "The N-terminus of the intrinsically disordered protein $\alpha$-synuclein triggers membrane binding and helix folding". In: *Biophysical Journal* 99.7, pp. 2116–2124. ISSN: 15420086. DOI: 10.1016/j.bpj.2010.06.035.

Brown, David R. (2010). *Oligomeric alpha-synuclein and its role in neuronal death.* DOI: 10.1002/iub.316.

Chinta, Shankar J and Julie K Andersen (2005). "Dopaminergic neurons". In: *The international journal of biochemistry & cell biology* 37.5, pp. 942–946.

Cremades, Nunilo et al. (2012). "Direct observation of the interconversion of normal and toxic forms of $\alpha$-synuclein". In: *Cell* 149.5, pp. 1048–1059. ISSN: 00928674. DOI: 10.1016/j.cell.2012.03.037. URL: http://dx.doi.org/10.1016/j.cell.2012.03.037.

Das, Payel, Silvina Matysiak, and Jeetain Mittal (2018). "Looking at the Disordered Proteins through the Computational Microscope". In: *ACS Central Science* 4.5, pp. 534–542. ISSN: 23747951. DOI: 10.1021/acscentsci.7b00626.

Dedmon, Matthew M. et al. (2005). "Mapping long-range interactions in $\alpha$-synuclein using spin-label NMR and ensemble molecular dynamics simulations". In: *Journal of the American Chemical Society* 127.2, pp. 476–477. ISSN: 00027863. DOI: 10.1021/ja044834j.

Fusco, Giuliana, Alfonso De Simone, Paolo Arosio, et al. (2016). "Structural Ensembles of Membrane-bound $\alpha$-Synuclein Reveal the Molecular Determinants of Synaptic Vesicle Affinity". In: *Scientific Reports* 6. ISSN: 20452322. DOI: 10.1038/srep27125.

Fusco, Giuliana, Alfonso De Simone, Tata Gopinath, et al. (2014). "Direct observation of the three regions in $\alpha$-synuclein that determine its membrane-bound behaviour". In: *Nature Communications* 5. ISSN: 20411723. DOI: 10.1038/ncomms4827.

Fusco, Giuliana, Tillmann Pape, et al. (2016). "Structural basis of synaptic vesicle assembly promoted by $\alpha$-synuclein". In: *Nature Communications* 7. ISSN: 20411723. DOI: 10.1038/ncomms12563.

Fusco, Giuliana, Maximo Sanz-Hernandez, and Alfonso De Simone (2018). "Order and disorder in the physiological membrane binding of $\alpha$-synuclein". In: *Current opinion in structural biology* 48, pp. 49–57.

Galvagnion, Cfffdfffdline et al. (2015). "Lipid vesicles trigger $\alpha$-synuclein aggregation by stimulating primary nucleation". In: *Nature Chemical Biology* 11.3, pp. 229–234. ISSN: 15524469. DOI: 10.1038/nchembio.1750.

Karplus, Martin and J Andrew McCammon (2002). "Molecular dynamics simulations of biomolecules". In: *Nature Structural & Molecular Biology* 9.9, p. 646.

Lautenschläger, Janin et al. (2018). "C-terminal calcium binding of $\alpha$-synuclein modulates synaptic vesicle interaction". In: *Nature Communications* 9.1. ISSN: 20411723. DOI: 10.1038/s41467-018-03111-4.

Lemkul, Justin (2018). "From Proteins to Perturbed Hamiltonians: A Suite of Tutorials for the GROMACS-2018 Molecular Simulation Package [Article v1. 0]". In: *Living Journal of Computational Molecular Science* 1.1, p. 5068.

Lindahl, Erik R (2008). "Molecular dynamics simulations". In: *Molecular modeling of proteins*. Springer, pp. 3–23.

Maltsev, Alexander S., Jinfa Ying, and Ad Bax (2012). "Impact of N-terminal acetylation of $\alpha$-synuclein on its random coil and lipid binding properties". In: *Biochemistry* 51.25, pp. 5004–5013. ISSN: 00062960. DOI: 10.1021/bi300642h.

Marrink, Siewert J. et al. (2019). *Computational Modeling of Realistic Cell Membranes*. DOI: 10.1021/acs.chemrev.8b00460.

Periole, Xavier and Siewert Jan Marrink (2013). "The martini coarse-grained force field". In: *Methods in Molecular Biology* 924, pp. 533–565. ISSN: 10643745. DOI: 10.1007/978-1-62703-17-5{_}20.

Periole, Xavier and Siewert-Jan Marrink (2013). "The Martini coarse-grained force field". In: *Biomolecular Simulations*. Springer, pp. 533–565.

Pettersen, Eric F et al. (2004). "UCSF Chimera–a visualization system for exploratory research and analysis." In: *Journal of computational chemistry* 25.13, pp. 1605–12. ISSN: 0192-8651. DOI: 10.1002/jcc.20084. URL: http://www.ncbi.nlm.nih.gov/pubmed/15264254.

Sang, Myun Park et al. (2002). "Distinct roles of the N-terminal-binding domain and the C-terminal-solubilizing domain of $\alpha$-synuclein, a molecular chaperone". In: *Journal of Biological Chemistry* 277.32, pp. 28512–28520. ISSN: 00219258. DOI: 10.1074/jbc.M111971200.

Tieleman, D. Peter et al. (2008). "The MARTINI Coarse-Grained Force Field: Extension to Proteins". In: *Journal of Chemical Theory and Computation* 4.5, pp. 819–834. ISSN: 1549-9618. DOI: 10.1021/ct700324x. URL: http://pubs.acs.org/doi/abs/10.1021/ct700324x.

Vamvaca, Katherina, Michael J. Volles, and Peter T. Lansbury (2009). "The First N-terminal Amino Acids of $\alpha$-Synuclein Are Essential for $\alpha$-Helical Structure Formation In Vitro and Membrane Binding in Yeast". In: *Journal of Molecular Biology* 389.2, pp. 413–424. ISSN: 00222836. DOI: 10.1016/j.jmb.2009.03.021.

Van Der Spoel, David et al. (2005). "GROMACS: Fast, flexible, and free". In: *Journal of Computational Chemistry* 26.16, pp. 1701–1718. ISSN: 01928651. DOI: 10.1002/jcc.20291.

Wang, Chuchu et al. (2016). "Versatile Structures of $\alpha$-Synuclein". In: *Frontiers in Molecular Neuroscience* 9.June, pp. 1–8. ISSN: 1662-5099. DOI: 10.3389/fnmol.2016.00048. URL: http://journal.frontiersin.org/Article/10.3389/fnmol.2016.00048/abstract.

# 6 Supplementary Material

## 6.1 Relative Binding Propensity for aminoacids sequence

**(a)** Del2 Helical

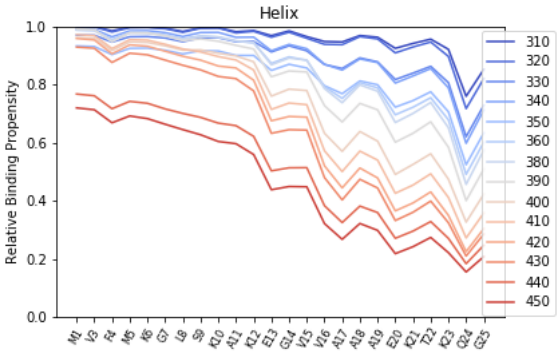


**(b)** Del2 Disordered

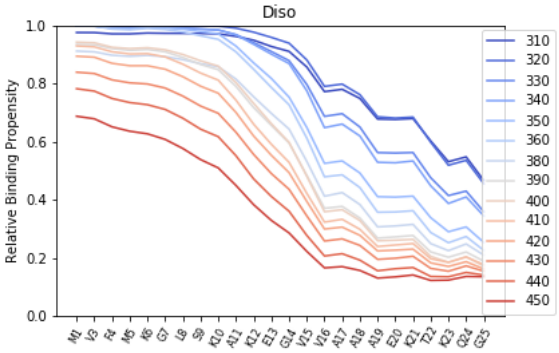


**Figure 20: Relative Binding Propensity for residues 1-25 in Del2.** Relative binding propensity is shown for the helical simulation (**a**)) and the disordered simulation (**b**)). Temperatures (K) for every simulation are shown with a colour-scale: blue colours represent lower temperatures and red colours show higher temperatures ranging from 310 to 450.

**(a)** Del2-3 Helical

**(b)** Del2-3 Disordered

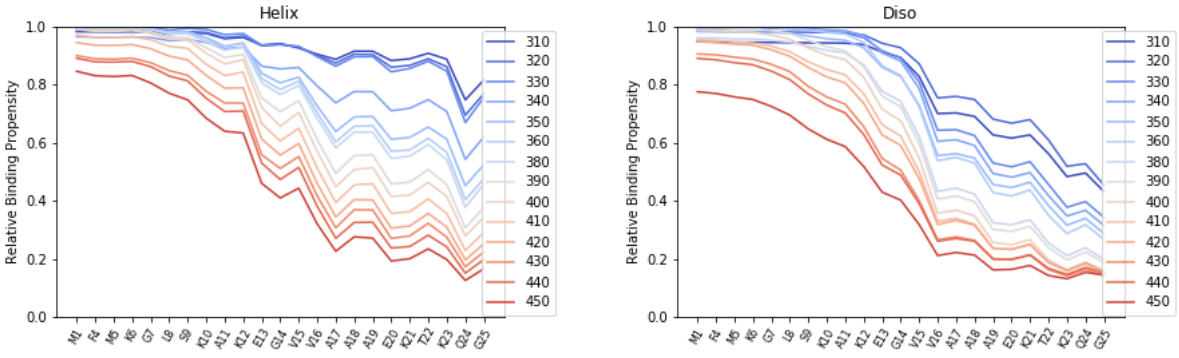


**Figure 21: Relative Binding Propensity for residues 1-25 in Del2-3.**

**(a)** Del2-4 Helical

**(b)** Del2-4 Disordered

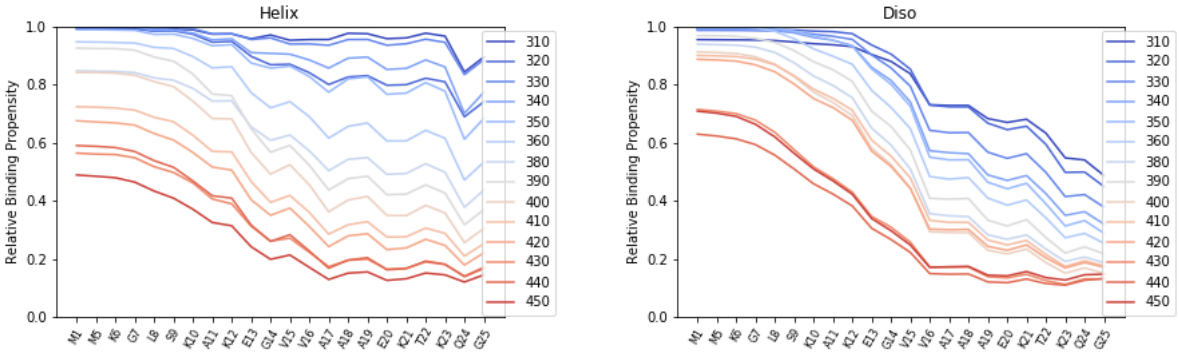


**Figure 22: Relative Binding Propensity for residues 1-25 in Del2-4.**

**(a)** Del2-5 Helical

**(b)** Del2-5 Disordered

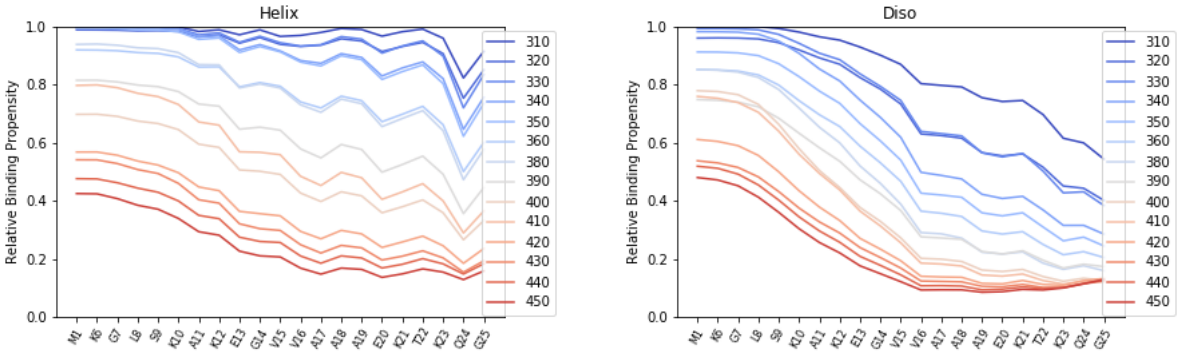


**Figure 23: Relative Binding Propensity for residues 1-25 in Del2-5.**

**(a)** Del2-7 Helical

**(b)** Del2-7 Disordered

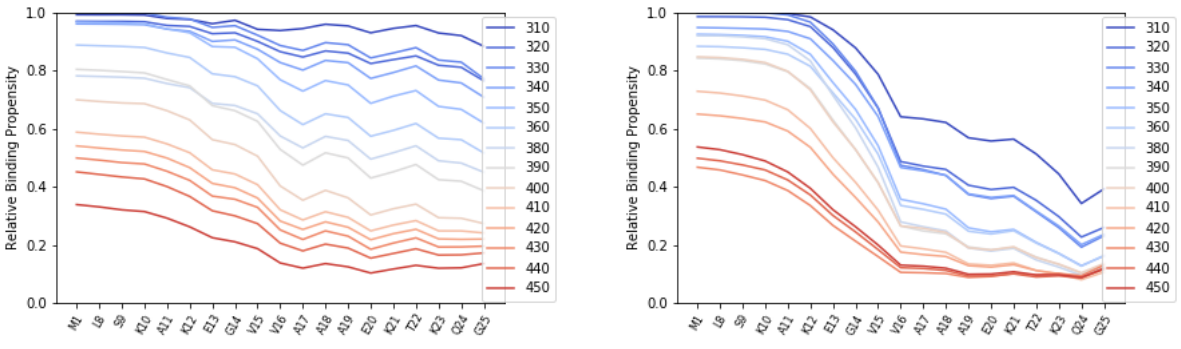


**Figure 24: Relative Binding Propensity for residues 1-25 in Del2-7.**

**(a)** Del2-11 Helical

**(b)** Del2-11 Disordered

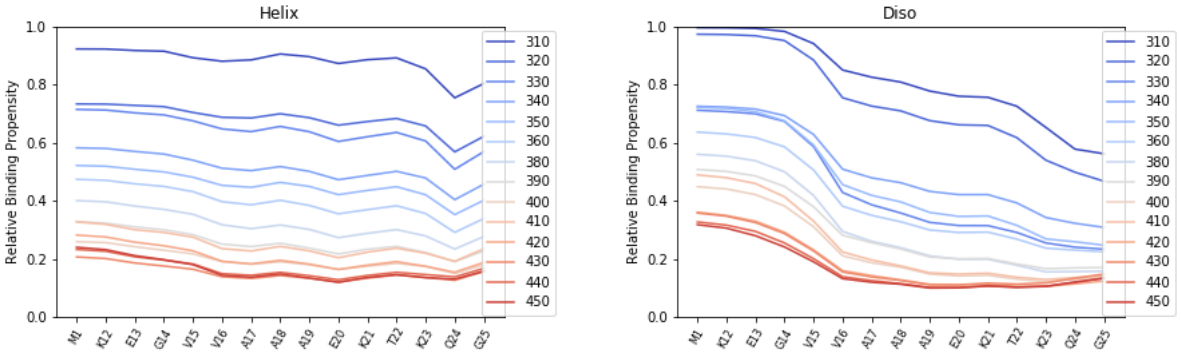


**Figure 25: Relative Binding Propensity for residues 1-25 in Del2-11.**

## 6.2 Comparison of Melting curves for different variants

**(a)** 1-11 Helical

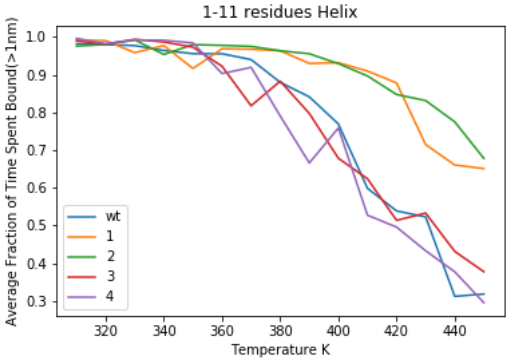


**(b)** 1-11 Disordered

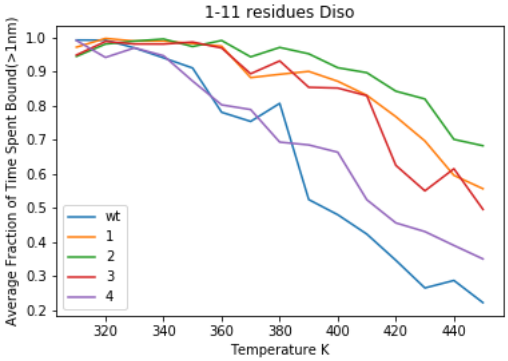


**(c)** 12-25 Helix

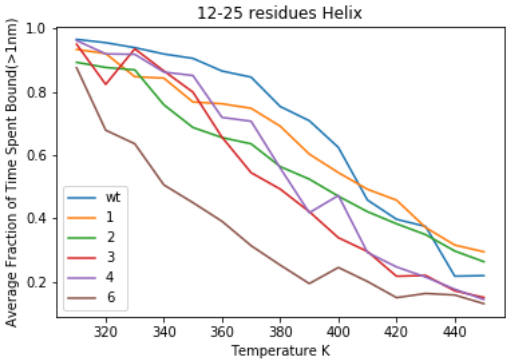


**(d)** 12-25 Disordered

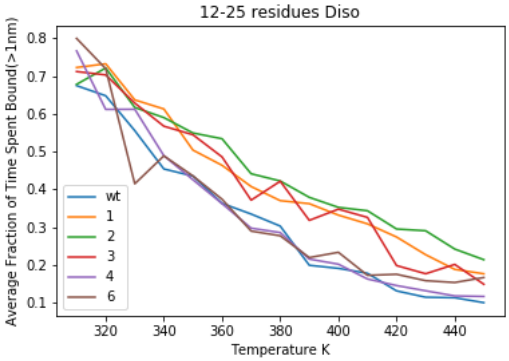


**Figure 26: Comparison of melting curves for alpha synuclein's variants and wild-type.** Wild type is shown in blue, Del2 is shown in orange, Del2-3 is shown in green, De2-4 is shown in red, Del2-5 is shown in purple and finally Del2-11 is shown in Brown.